Energy Reports 15 (2026) 109180

Contents lists available at ScienceDirect

Energy Reports

journal homepage: www.elsevier.com/locate/egyr

Research paper

Resilience enhancement for distribution networks: Co-deployment of mobile energy storage systems and EV charging stations in strong wind events

Jie Ma, Youwen Zhang *, Changqing Xu, Yong Guo, Yihao Sun

Planning Review Center, State Grid Economic and Technological Research Institute of Henan Province, Zhengzhou 450006, China

ARTICLE INFO

Keywords:
Distribution network
Mobile energy storage system
Electric vehicle charging station
Resilience improvement

ABSTRACT

To address the challenge of ineffective critical load restoration during extreme strong wind events due to insufficient pre-disaster resource allocation in distribution networks, this study aims to enhance distribution network resilience through a novel method that integrates pre-disaster preventive measures with in-disaster island merging under high-wind conditions. First, the spatiotemporal evolution characteristics of strong winds are analyzed using the power-law wind profile model to determine the time-varying failure rates of distribution lines. Typical fault scenarios under strong wind weather are then generated via Monte Carlo simulation. Second, an optimization model is developed for pre-disaster distribution line reinforcement and mobile energy storage system (MESS) pre-deployment. For the generated fault scenarios, an in-disaster restoration model incorporating island merging is established, which explicitly formulates dynamic constraints coupling virtual power flows with the state variables of network nodes and branches. A dynamic MESS dispatching strategy is also introduced to collaboratively restore load supply with pre-deployed electric vehicle charging stations (EVCS). Finally, simulation results on the IEEE 33-node test system validate that the proposed strategy successfully secures the power supply to critical loads and improves system resilience.

1. Introduction

Recently, the increasing frequency of extreme natural disasters has caused severe damage to power systems, resulting in widespread power outages and significant economic losses (Qiu et al., 2023; Liu et al., 2022; Shabani et al., 2025; Zhou et al., 2025a). This is particularly evident in distribution networks located in plain areas, where extreme wind events often lead to the toppling of trees along line corridors and the entanglement of foreign objects, causing line trips and regional power interruptions that pose serious threats to both residential living and agricultural production. Although continuous grid infrastructure upgrades have improved system resilience, efficiently restoring power under a large number of fault scenarios, particularly in maintaining supply to critical loads, remains a major challenge (Zhu et al., 2025; Sabouhi et al., 2021; Xu and Guo, 2024). As the final stage of electricity delivery, distribution systems are characterized by their high susceptibility to cascading failure effects and significant socio-economic repercussions when outages occur. Therefore, optimizing pre-disaster resource allocation and developing multi-source coordinated restoration strategies during disasters are essential to constructing a highly resilient distribution network (Wang et al., 2023; Li et al., 2023; Meng et al., 2025).

The three temporal phases of pre-disaster prevention, during-disaster response, and post-disaster recovery form a comprehensive framework for resilience improvement in distribution networks (He et al., 2025; Xu et al., 2025; Zhao et al., 2024). The pre-disaster prevention phase involves formulating differentiated defense strategies based on spatio-temporal disaster probability models, encompassing both long-term planning and short-term emergency preparedness measures (He et al., 2025). The during-disaster response phase implements network reconfiguration and island merging for critical loads through rational network splitting and switching operations (Xu et al., 2025). The post-disaster recovery phase primarily employs centralized power supply strategies to minimize distribution system outage losses. Compared with post-disaster recovery capabilities, coordinated resilience improvement focusing on the pre-disaster prevention and during-disaster response phases proves more effective in reducing outage risks for critical loads (Saif et al., 2023).

* Corresponding author.
E-mail address: 630091030@qq.com (Y. Zhang).

https://doi.org/10.1016/j.egyr.2026.109180
Received 9 December 2025; Received in revised form 5 February 2026; Accepted 7 March 2026
Available online 18 March 2026

Pre-disaster prevention primarily involves short-term emergency strategies, including the optimization of distribution network structures and construction standards, the enhancement of disaster resilience for critical power facilities, and the upgrading or replacement of aging equipment (Abbasi and Seifi, 2015). Reference (Ziari et al., 2012) proposes a preventive planning method based on the coordinated configuration of conventional equipment upgrades and controllable distributed generators (DDGs). It develops a comprehensive resilience improvement framework comprising three levels: capacitor optimization, voltage regulation, and line upgrades. Recent studies have extended resilience-oriented planning in active distribution networks toward the coordinated deployment of distributed generation and energy storage, providing flexible operational support beyond conventional equipment reinforcement strategies (Wang et al., 2023; Li et al., 2018a, 2022). However, relying exclusively on planning-based reinforcement measures offers limited effectiveness in improving distribution network resilience, often requires substantial financial investment, and may result in economic inefficiency.

Mobile energy storage systems (MESS) are widely utilized for enhancing distribution network resilience owing to their rapid response, flexibility, and operational convenience (Chen et al., 2022). Based on pre-disaster hazard information, references (Zhou et al., 2023; Shi et al., 2023) optimized the spatial deployment and quantity allocation of MESS, leveraging its flexibility to effectively reduce load restoration time in outage areas, thereby improving system resilience. These studies collectively validate the significant advantages of MESS features such as high flexibility and dispatch convenience during the pre-disaster prevention stage. Furthermore, pre-deployed electric vehicle charging stations (EVCS) at critical nodes can serve as fixed distributed storage units during extreme weather events, supporting critical loads by injecting power into the distribution network via a controlled discharge mode (Li et al., 2021). The viability of this concept is supported by studies on dispatchable electric vehicle infrastructure in isolated systems, such as islanded microgrids (Najafi et al., 2021; Li et al., 2018b). This creates a complementary “fixed-mobile” advantage in power supply characteristics when combined with MESS (Meng et al., 2024). However, existing research on MESS predominantly focuses on static pre-disaster configuration, often neglecting the impact of dispatch time on distribution networks, which limits the full exploitation of MESS’s potential for dynamic resilience improvement across multiple time scales (El-Sayed et al., 2025).

During the in-disaster response phase, primary measures include network reconfiguration, emergency islanding, and real-time dispatch of mobile power sources, among others. Network reconfiguration adjusts the network topology through switching operations to isolate faulted areas and restore power to non-faulted sections (Hao et al., 2025). Islanded operation relies on distributed generator (DG) with black-start capability to form independent power islands that maintain the supply to critical loads (Gupta et al., 2021). Mobile power sources, such as rapidly deployable MESS or generator trucks, provide dynamic power support to these islands (Wu et al., 2022). Furthermore, EVCS, pre-deployed at key nodes, can serve as fixed distributed resources, providing emergency power support to local loads during disasters and functionally complementing mobile power sources (Huang et al., 2022). Reference (Lei et al., 2020) proposed a topological reconfiguration constraint model to enhance distribution network resilience; this model significantly expands the feasible solution space and improves solution quality during reconfiguration by enhancing topological flexibility. Reference (Peng et al., 2024) develops an island partitioning model employing depth-first and breadth-first search algorithms, incorporates conditional value at risk (CVaR) for risk quantification and dynamic optimization, and achieves efficient restoration of critical loads under extreme disasters. Reference (Li et al., 2025) establishes a mobile emergency power supply dispatch model that considers load importance and extreme weather impacts, aiming to minimize the cost associated with weighted load shedding during fault conditions. Most current studies primarily focus on island partitioning and network reconfiguration. Furthermore, they neither consider utilizing DGs for island merging to further expand the supply range, nor fully exploit the support potential of fixed distributed resources like EVCS. This leads to a lower power supply restoration rate under strong wind disasters, urgently necessitating the establishment of an in-disaster dynamic island merging and multi-source coordinated optimization model to enhance system resilience.

The aforementioned studies collectively validate the effectiveness of pre-disaster line hardening, MESS pre-deployment, and in-disaster service restoration in enhancing distribution network resilience. However, they failed to establish a multi-stage coordinated optimization framework to fully leverage their potential. In recent years, some research has attempted to integrate coordinated strategies such as "pre-post-disaster", "in-post-disaster", or "pre-in-disaster" to enhance resilience. Reference (Zhou et al., 2025b) proposed a two-stage distribution network resilience improvement strategy for extreme disasters like heavy wind and rain. It employs the K-means clustering algorithm and Monte Carlo simulation to generate fault scenarios and establishes a stochastic optimization model combining pre-disaster line hardening, DG deployment, and post-disaster network reconfiguration and line repair. Reference (Qin et al., 2024) presented a two-stage method involving pre-disaster optimal resource deployment and post-disaster coordinated resource dispatch for wind-flood compound disasters to improve distribution network restoration capability. Reference (Shi et al., 2022) developed an in-post-disaster two-stage coordinated method for distribution network resilience improvement by coordinating DG dispatch, network topology reconfiguration, and repair crew scheduling. While these studies strengthen the disaster resilience of distribution networks against extreme weather through a multi-stage coordination of measures, the existing "pre-in-disaster" coordination strategies generally fail to integrate the fixed support capability of EVCS with the cross-time-scale dynamic dispatch process of MESS and island merging measures, which limits further enhancement of distribution network resilience.

Therefore, to address the limitations of existing strategies, this paper formulates a generic optimization method for enhancing distribution network resilience that considers pre-disaster planning and in-disaster island merging. The substantive incremental contributions of this work are twofold: First, it establishes a “fixed-mobile” multi-source coordinated resilience mode. The pre-disaster stage involves a coordinated deployment scheme for line hardening, MESS, and EVCS, leveraging the localized support of EVCS to complement the spatiotemporal flexibility of MESS. Second, it realizes the deep coupling of island “partitioning-merging” and dynamic dispatch. The in-disaster stage coordinately considers DG-based island partitioning and merging, implementing rapid service restoration based on cross-time-scale MESS dynamic dispatch. Finally, while this study utilizes a strong wind model for validation, the proposed coordinated framework possesses inherent scalability, allowing for extension to other extreme disaster scenarios by adapting the disaster-specific fault generation module. This achieves joint decision-making for preventive resource deployment and fault recovery strategies, reducing the system load loss and improving both system resilience and economic efficiency.

2. Island partition and merging utilizing black-start DG

In the virtual network model constructed based on the single-commodity flow concept (Alizadeh et al., 2024), the virtual power flow characterizes the electrical energy transmission process in a power system under islanded operation. In this model, the process of supplying energy from black-start-capable DG to de-energized zones is equivalent to the power transmission from source nodes to load nodes in the virtual network, with its transmission characteristics defined by the virtual power flow values. The distribution of the virtual power flow depends on the virtual network structure, the virtual power output from DG, and the load distribution in the de-energized zones. With a focus on swift recovery of the distribution grid, the virtual power flow must be optimally allocated while satisfying constraints such as DG output limits, radial topology requirements, and supply priorities for de-energized zones, thereby guiding the development of island partitioning and restoration strategies for the actual distribution network.

2.1. Virtual power flow constraints for island partitioning

A differentiated modeling approach for the virtual power flow constraints in distribution network island partitioning is adopted based on the connection status of DG. System nodes are categorized into two types: ordinary nodes and black-start DG nodes. The former must satisfy the power balance constraint based on the virtual topology, given by Eq. (1), while the latter must comply with the coupling constraint between the DG output characteristics and the virtual network topology, expressed in Eq. (2). This coupling constraint effectively captures the supporting role of black-start DG regulation capability in the island reconfiguration process, ensuring the feasibility of the virtual power flow under islanded operation.

$$\sum_{i\in Ls(i,:)} \overline{P}_{ij,t} - \sum_{i\in Le(:,i)} \overline{P}_{ki,t} = -1, \forall i \notin \Omega_{\mathrm{DG}}, \forall t \in \Omega_{\mathrm{t}} \tag{1}$$

$$\sum_{i\in Ls(i,:)} \overline{P}_{ij,t} - \sum_{i\in Le(:,i)} \overline{P}_{ki,t} = \overline{P}_{i,t}^{\mathrm{DG}}, \forall i \in \Omega_{\mathrm{DG}}, \forall t \in \Omega_{\mathrm{t}} \tag{2}$$

where, $Ls(i,:)$ represents the collection of to bus of the branch that flows out of node i; $Le(:,i)$ represents the collection of from bus of the branch that flows into node i; $\overline{P}_{ij,t}$ and $\overline{P}_{ki,t}$ represent the virtual power flows of line ij and line ki in period t respectively; $\overline{P}_{i,t}^{\mathrm{DG}}$ is the net virtual power injected by black start node DG of node i in period t; Ω_{DG} represents the collection of black start nodes DG; Ω_{t} is the set of time periods.

2.2. Virtual power flow constraints for island merging

(1) Virtual power flow constraints within partitioned areas

A node state variable $\sigma_{i,t}$ is introduced to allow island merging between different islands through switching operations, thereby forming a larger power supply area.

$$\sum_{i\in Le(:,i)} \overline{P}_{ki,t} - \sum_{i\in Ls(i,:)} \overline{P}_{ij,t} = \sigma_{i,t}, \forall i \notin \Omega_{\mathrm{DG}}, \forall t \in \Omega_{\mathrm{t}} \tag{3}$$

where, $\sigma_{i,t}$is a binary state variable representing the connectivity status of node i, $\sigma_{i,t} = 1$ indicates that node i is powered on during period t.

(2) Coupling constraints between virtual power flow and line connectivity states

The dependence of virtual power flow on line connectivity states is established using the big-M method.

$$-MZ_{ij,t} \le \overline{P}_{ij,t} \le MZ_{ij,t}, \forall ij \in \Omega_{\mathrm{line}}, \forall t \in \Omega_{\mathrm{t}} \tag{4}$$

where, $Z_{ij,t}$ is a binary variable representing the connectivity status of the t-period line ij, $Z_{ij,t} = 1$ indicates that the t-period line ij is connected, otherwise it is disconnected; Ω_{line} is the set of all lines; M is chosen as a sufficiently large positive constant, which is taken as 1×10^4 in this article.

(3) Constraints for de-energized zones

An auxiliary variable is defined, the value of which is influenced by both the line connectivity status and the corresponding node states. This auxiliary variable is used to restrict disconnected branches within the outage area from having virtual power flow, thereby enabling refined control over the de-energized zone.

$$\lambda_{ij,t} = \sigma_{i,t}\sigma_{j,t}Z_{ij,t}, \forall ij \in \Omega_{\mathrm{line}}, \forall i \in \Omega_{\mathrm{bus}}, \forall t \in \Omega_{\mathrm{t}} \tag{5}$$

$$\overline{P}_{ij,t} = \begin{cases} 0, \lambda_{ij,t} = 0 \\ \overline{P}_{ij,t}, \lambda_{ij,t} = 1 \end{cases}, \forall ij \in \Omega_{\mathrm{line}}, t \in \Omega_{\mathrm{t}} \tag{6}$$

where, Ω_{bus} is a set of distribution network nodes.

(4) Radial topology constraints for island areas

It is imperative that a radial topology be preserved in the distribution network throughout islanding and merging operations.

$$Z_{ij,t} = a_{ij,t} + a_{ji,t}, \forall ij \in \Omega_{\mathrm{line}}, \forall t \in \Omega_{\mathrm{t}} \tag{7}$$

$$\sum_{ij\in\Omega_{\mathrm{line}}} a_{ij,t} \le 1, \forall j \in \Omega_{\mathrm{bus}}, \forall t \in \Omega_{\mathrm{t}} \tag{8}$$

where, $a_{ij,t}$ and $a_{ji,t}$ are auxiliary 0–1 variables, if $a_{ij,t}$= 1 and $a_{ji,t}$= 0,then node i in t period is considered to be the parent node of node j, $a_{ij,t}$= 0 and $a_{ji,t}$= 1, node i in t period is not the parent node of node j.

3. Distribution line failure rate model under strong wind conditions

3.1. Strong wind field modelling

Strong wind events are typically induced by mesoscale weather processes such as extratropical cyclones, cold fronts, or intense convective systems. Unlike typhoons with distinct eyewall structures, such winds exhibit relatively gentle horizontal gradients but pronounced vertical wind speed variations, which critically influence the loads on vertical structures like distribution line towers.

To accurately calculate the wind load acting on distribution lines, wind speeds at the actual heights of conductors and towers must be determined. The characterization of mean wind speed variation utilizes the power-law wind profile model in engineering practice, representing speed as a function of height. This model is valued for its simplicity, clear physical interpretation, and inclusion in most structural load specifications.

The expression for the power-law wind profile model is given by:

$$V\left(z,t\right) = V_g(t)\cdot\left(\frac{z}{z_g}\right)^{\alpha} \tag{9}$$

where, $V(z,t)$ is the mean wind speed measured at an elevation of z at time t; $V_g(t)$ corresponds to the mean wind speed at the reference height z_g at time t; z_g is set to 10 m following conventional meteorological measurement practice; α is the wind profile exponent. The wind profile exponent α serves as a critical parameter characterizing the weakening effect of surface friction on wind speed, and its value depends on the terrain type along the line corridor. The values of α corresponding to different ground roughness categories are listed in Table 1.

The time-varying characteristics of the strong wind process are represented by the time-varying wind speed sequence $V_g(t)$ at the reference height. This data can be sourced from historical records of extreme weather events or predictions from numerical weather prediction models. Using Eq. (9), $V_g(t)$ can be converted to the temporal variation of wind speed $V(z,t)$ at the heights of the distribution lines and towers, thereby providing dynamic input for the subsequent calculation of time-varying wind loads and time-varying failure rates. It is important to acknowledge that the power-law wind profile model characterizes the

Table 1
Values of the wind profile exponent.

Ground Category	Value of α
Open sea, lake surface, desert	0.12
Fields, countryside, jungle	0.16
Suburbs, small towns	0.22
Urban center, dense high-rise areas	0.30

spatiotemporal evolution of mean wind speeds. In practical engineering applications, prediction errors or abrupt wind speed changes are inevitable. In this study, this model serves as a physical baseline for generating stochastic fault scenarios. The potential impact of these uncertainties is subsequently mitigated by the proposed two-stage coordinated framework, where the in-disaster dynamic dispatch of MESS and EVCS acts as a real-time corrective mechanism to adapt to deviations between the predicted and realized wind conditions.

3.2. Distribution line failure rate calculation model

(1) Wind load calculation

The calculation formulas for wind loads F_l and F_p on distribution lines and towers are given by Eq. (10).

$$\begin{cases} F_l = \varepsilon\mu_z\mu_{sc}dl_{\mathrm{H}}\sin^2\varphi_{\mathrm{x}}\dfrac{v^2(t)}{1600} \\ F_p = \gamma\mu_z\mu_s A\dfrac{v^2(t)}{1600} \end{cases} \tag{10}$$

where, $v(t)$ corresponds to the wind speed at the location of the line during period t; ε,γ,φ_{x},μ_z,μ_{sc} and μ_s are the wind load heterogeneity coefficient, wind-induced vibration coefficient, wind deviation angle, wind pressure variation coefficient with height, conductor drag coefficient, and wind load shape coefficient, respectively; d, l_{H} and A are the conductor outer diameter, tower horizontal span and tower shape coefficient respectively.

(2) Distribution line and tower failure rate models

The strength of components such as distribution lines and towers is generally considered to obey the normal distribution, as shown in Eq. (11). The component function is defined as the difference between the external load and its intensity. When the difference is considered to be greater than 0, it indicates that the component operation is unreliable, as shown in Eq. (12), and the probabilities of line failure and tower failure are given by Eq. (13):

$$f(R) = \frac{1}{\sqrt{2\pi}\delta}e^{-\frac{1}{2}\left(\frac{R-\mu}{\delta}\right)^2} \tag{11}$$

$$P = P\{F - R > 0\} \tag{12}$$

$$\begin{cases} P_l^k = \displaystyle\int_0^S \frac{1}{\sqrt{2\pi}\delta_l}e^{-\frac{1}{2}\left(\frac{R_l-\mu_l}{\delta_l}\right)^2}\mathrm{d}R \\ P_p^k = \displaystyle\int_0^S \frac{1}{\sqrt{2\pi}\delta_p}e^{-\frac{1}{2}\left(\frac{R_p-\mu_p}{\delta_p}\right)^2}\mathrm{d}R \end{cases} \tag{13}$$

where, R is the strength of the component itself; F characterizes the mechanical load applied to the distribution line or the bending moment exerted on the tower; δ and μ represent the average value and statistical dispersion of the bending strength, respectively; P_l^k and P_p^k are the failure rates of the lines and towers, respectively; R_l and R_p are the own strength of the lines and towers; δ_l, δ_p, μ_l and μ_p represent the average value and statistical dispersion of the bending strength of the lines and towers, respectively.

(3) Overall failure rate model of distribution lines

When a distribution line fails, it is considered that the line fails when any component of the conductor or tower fails. Consequently, the series model is employed to determine the probability of a line failure.

$$P_{all}^{k,i} = 1 - \prod_{k=1}^{Q_1}(1 - P_l^{k,i})\prod_{k=1}^{Q_2}(1 - P_p^{k,i}) \tag{14}$$

where, $P_{all}^{k,i}$, $P_l^{k,i}$ and $P_p^{k,i}$ are respectively the overall failure probability, tower and conductor failure probability of the i distribution line; Q_1 and Q_2 are respectively the number of pole towers and conductor spans in the line.

3.3. Extreme scene construction

Based on the calculated overall failure rate of distribution lines, this paper uses Monte Carlo random sampling to generate a set of typical scenarios under extreme strong wind weather Θ :

$$\Theta = \{\sum_{ij\in\Omega_{\mathrm{line}}}(1 - u_{ij,t}) \le \Gamma, u_{ij,t} \in \{0,1\}, \forall ij \in \Omega_{\mathrm{line}}, \forall t \in \Omega_{\mathrm{t}}\} \tag{15}$$

where, $u_{ij,t}$ is a 0–1 status variable indicating whether the line is affected by natural disasters, $u_{ij,t} = 0$ means that the line is faulty due to the strong wind, $u_{ij,t} = 1$ means that the line is normal; Γ is the maximum number of lines affected by natural disasters.

To ensure the representativeness of the generated scenarios and minimize the sensitivity of the results to the sample size, the simulation was conducted with a sufficiently large number of iterations to approximate the true probability distribution of faults. Compared to deterministic approaches or data-driven methods that rely heavily on scarce historical records of extreme events, the Monte Carlo method is selected here for its robustness in capturing the continuous stochastic characteristics of wind-induced failures, thereby ensuring the reliability of the subsequent optimization.

4. Optimization model for distribution network resilience improvement under strong wind disasters

This work formulates an optimization model for enhancing distribution network resilience that considers both pre-disaster planning and in-disaster island merging. The pre-disaster planning component is used to select distribution line reinforcement locations and MESS pre-deployment positions. The in-disaster service restoration component performs island partitioning and merging through black-start DG and switching operations, while conducting coordinated dispatch of pre-deployed EVCS and MESS to restore the distribution network after faults.

4.1. Objective function

A cost-optimization model is developed to achieve the minimum total system cost, which consists of pre-event investment and post-event recovery expenditures:

$$\min(F_{\mathrm{ivs}} + F_{\mathrm{rec}}) \tag{16}$$

where, F_{ivs} and F_{rec} represent the pre-disaster planning cost and the in-disaster restoration cost, respectively.

The pre-disaster planning cost includes line reinforcement costs and fixed MESS costs, as expressed in Eq. (17).

$$\begin{cases} F_{\mathrm{ivs}} = F_{\mathrm{inv}}^{\mathrm{line}} + F_{\mathrm{fix}}^{\mathrm{MESS}} \\ F_{\mathrm{ivs}}^{\mathrm{line}} = \displaystyle\sum_{ij\in\Omega_{\mathrm{line}}} c_{\mathrm{h}}L_{ij}^{\mathrm{ew}}y_{ij} \\ F_{\mathrm{fix}}^{\mathrm{MESS}} = c_{\mathrm{fix}}X^{\mathrm{MESS}} \end{cases} \tag{17}$$

where, $F_{\mathrm{ivs}}^{\mathrm{line}}$ and $F_{\mathrm{fix}}^{\mathrm{MESS}}$ are line reinforcement costs and MESS fixed costs respectively; y_{ij} is the status of line ij reinforcement, $y_{ij} = 1$ means reinforced linesij, $y_{ij}=0$ means not reinforced; X^{MESS} is the number of pre-deployed MESS; c_{h} and c_{fix} are line reinforcement costs per unit length and MESS fixed costs respectively; L_{ij}^{ew} is the length of line ij.

The in-disaster restoration cost consists of the minimized load shedding cost, line switching operation cost, EVCS discharging cost, MESS discharging cost, and MESS mobility cost under extreme scenario d, as given in Eq. (18):

$$\begin{cases} F_{\text{rec}}=\sum\limits_{d\in\Theta}\pi_d\Big(F_{\text{loss},d}+F_{\text{S},d}+F_{\text{dis},d}^{\text{EVCS}} \\ \qquad +F_{\text{dis},d}^{\text{MESS}}+F_{\text{mov},d}^{\text{MESS}}\Big) \\ F_{\text{loss},d}=\sum\limits_{i\in\Omega_{\text{bus}}}\sum\limits_{t\in\Omega_{\text{t}}}\Big[\left(1-\sigma_{i,d,t}\right)\Big(c_{\text{loss1}}P_{i,d,t}^{\text{l1}}+ \\ c_{\text{loss2}}P_{i,d,t}^{\text{l2}}+c_{\text{loss3}}P_{i,d,t}^{\text{l3}}\Big)\Big] \\ F_{\text{S},d}=\sum\limits_{ij\in\Omega_{\text{tie}}}\sum\limits_{t\in\Omega_{\text{t}}}c_{\text{tie}}\left(S_{ij,d,t}^{\text{open}}+S_{ij,d,t}^{\text{close}}\right)+ \\ \sum\limits_{ij\in\Omega_{\text{sec}}}\sum\limits_{t\in\Omega_{\text{t}}}c_{\text{sec}}\left(S_{ij,d,t}^{\text{open}}+S_{ij,d,t}^{\text{close}}\right) \\ F_{\text{dis},d}^{\text{EVCS}}=\sum\limits_{i\in\Omega_{\text{bus}}}\sum\limits_{t\in\Omega_{\text{t}}}c_{\text{dis}}^{\text{EVCS}}P_{i,d,t}^{\text{EVCS}} \\ F_{\text{dis},d}^{\text{MESS}}=\sum\limits_{m\in\Omega_{\text{MESS}}}\sum\limits_{i\in\Omega_{\text{bus}}}\sum\limits_{t\in\Omega_{\text{t}}}c_{\text{dis}}P_{m,i,d,t}^{\text{MESS}} \\ F_{\text{mov},d}^{\text{MESS}}=\sum\limits_{m\in\Omega_{\text{MESS}}}\sum\limits_{i\in\Omega_{\text{bus}}}\sum\limits_{j\in\Omega_{\text{bus}}}\sum\limits_{t=1}^{T-\Delta t_{m,i,j}-1} \\ c_{\text{mov}}\left(x_{m,i,d,t}x_{m,j,d,t+\Delta t_{m,i,j}+1}L_{i,j}^{\text{rou}}\right) \end{cases} \tag{18}$$

where, Ω_{MESS} is MESS collection;$F_{\text{loss},d}$, $F_{\text{S},d}$, $F_{\text{dis},d}^{\text{EVCS}}$, $F_{\text{dis},d}^{\text{MESS}}$ and $F_{\text{mov},d}^{\text{MESS}}$ are respectively the load loss cost, line switch action cost, EVCS discharge cost, MESS discharge cost and MESS movement cost under the extreme scenario d, of which $F_{\text{mov},d}^{\text{MESS}}$ are related to the movement path; π_d is the probability of occurrence of the extreme scenario d; Ω_{tie} and Ω_{sec} are the tie switch set and the segmented switch set respectively; c_{loss1}, c_{loss2} and c_{loss3} are the unit load loss costs of the primary load, the secondary load and the tertiary load respectively; c_{tie} and c_{sec} are the contact switch and segmented switch action costs respectively; $c_{\text{dis}}^{\text{EVCS}}$ is unit discharge cost of EVCS; c_{mov} and c_{dis} represent the unit distance movement cost and unit discharge cost of MESS respectively; $S_{ij,d,t}^{\text{open}}$ and $S_{ij,d,t}^{\text{close}}$ are the switching action variables of line ij in period t under extreme scenario d; $P_{i,d,t}^{\text{l1}}$, $P_{i,d,t}^{\text{l2}}$ and $P_{i,d,t}^{\text{l3}}$ represent the active power of next-level load, second-level load and third-level load in extreme scenario d respectively; $P_{i,d,t}^{\text{EVCS}}$ is the discharge power of EVCS at node i during period t under extreme scenario d;; $P_{m,i,d,t}^{\text{MESS}}$ is the discharge power of MESS m at node i during period t under extreme scenario d;$T$is the time scale, this paper takes $T=24$; $L_{i,j}^{\text{rou}}$is the MESS scheduling path from node i to node j. $x_{m,i,d,t}$ is the status of the MESS m being scheduled at the i node in the t period under the extreme scenario d. $x_{m,i,d,t}$= 1 means it is scheduled at the i node, and $x_{m,i,d,t}$= 0 means it is not scheduled at the i node; $\Delta t_{m,i,j}$ is the shortest travel time for the MESS m from node i to node j, which is determined by the inter-node distance $L_{i,j}^{\text{rou}}$ and MESS moving speed v_m.

$$\Delta t_{m,i,j}=L_{i,j}^{\text{rou}}\Big/v_m \tag{19}$$

4.2. Constraints

(1) Line reinforcement quantity constraints

$$\sum_{ij\in\Omega_{\text{line}}}y_{ij}\le y_{\max} \tag{20}$$

where, $y_{\max}$ defines the maximum allowable quantity of reinforced lines.

(2) MESS deployment quantity constraints

$$X^{\text{MESS}}=\sum_{m\in\Omega_{\text{MESS}}}\sum_{i\in\Omega_{\text{bus}}}x_{m,i,0} \tag{21}$$

$$X^{\text{MESS}}\le X_{\max}^{\text{MESS}} \tag{22}$$

$$\sum_{i\in\Omega_{\text{bus}}}x_{m,i,0}\le 1,\forall m\in\Omega_{\text{MESS}} \tag{23}$$

where, $x_{m,i,0}$is the state variable of node i at the initial deployment location of MESS m. If $x_{m,i,0}=0$, it means that the system does not deploy MESS m; $X_{\max}^{\text{MESS}}$ is the number of MESS in the area.

Eq. (21) represents the relationship between the pre-deployment status $x_{m,i,0}$ and the pre-deployment quantity X^{MESS}; Eq. (22) indicates that the number of pre-deployed MESS does not exceed the number of MESS in the area; Eq. (23) indicates that each MESS to be pre-deployed at most on one node.

(3) Electric vehicle charging station constraints

$$0\le P_{i,d,t}^{\text{EVCS}}\le x_i{}^{\text{EVCS}}\cdot P^{\text{EVCS, max}} \tag{24}$$

$$-x_i{}^{\text{EVCS}}\cdot Q^{\text{EVCS, max}}\le Q_{i,d,t}^{\text{EVCS}}\le x_i{}^{\text{EVCS}}\cdot Q^{\text{EVCS, max}} \tag{25}$$

$$\sum_t^T P_{i,d,t}^{\text{EVCS}}\cdot\Delta t\le E^{\text{EVCS, max}} \tag{26}$$

$$\sqrt{\left|P_{i,d,t}^{\text{EVCS}}\right|^2+\left|Q_{i,d,t}^{\text{EVCS}}\right|^2}\le S^{\text{EVCS, max}} \tag{27}$$

where, $P_{i,d,t}^{\text{EVCS}}$ and $Q_{i,d,t}^{\text{EVCS}}$ correspond to the real and reactive power delivered by the EVCS at node i during period t under extreme scenario d, respectively; $x_i{}^{\text{EVCS}}$ is a binary state variable for EVCS deployment at node i, with $x_i{}^{\text{EVCS}}=1$ indicating deployment and $x_i{}^{\text{EVCS}}=0$ indicating no deployment; $P^{\text{EVCS, max}}$ and $Q^{\text{EVCS, max}}$ denote the maximum allowable real and reactive power output from the EVCS; $E^{\text{EVCS, max}}$ specifies the maximum energy the EVCS can deliver over the restoration period;$S^{\text{EVCS, max}}$ defines the capacity upper limit of the EVCS.

(4) Distribution network power flow constraints

The node state variable $\sigma_{i,t}$ and the line state variable $Z_{ij,t}$ are introduced into the Distflow power flow model (Qian et al., 2025), expressed as :

$$\begin{cases} P_{i,d,t}^{\text{in}}=\sum\limits_{ij\in\Omega_{\text{line}}}P_{ij,d,t}-\sum\limits_{ki\in\Omega_{\text{line}}}\left(P_{ki,d,t}-R_{ki}I_{ki,d,t}^2\right) \\ Q_{i,d,t}^{\text{in}}=\sum\limits_{ij\in\Omega_{\text{line}}}Q_{ij,d,t}-\sum\limits_{ki\in\Omega_{\text{line}}}\left(Q_{ki,d,t}-X_{ki}I_{ki,d,t}^2\right) \end{cases}, \\ \forall i\in\Omega_{\text{bus}},\forall t\in\Omega_{\text{t}},\forall d\in\Theta \tag{28}$$

$$V_{i,d,t}^2-V_{j,d,t}^2=2(P_{ij,d,t}R_{ij}+Q_{ij,d,t}X_{ij})- \\ I_{ij,d,t}^2(R_{ij}^2+X_{ij}^2), \\ \forall i\in\Omega_{\text{bus}},\forall ij\in\Omega_{\text{line}},\forall t\in\Omega_{\text{t}},\forall d\in\Theta \tag{29}$$

$$I_{ij,d,t}^2V_{i,d,t}^2=P_{ij,d,t}^2+Q_{ij,d,t}^2, \\ \forall ij\in\Omega_{\text{line}},\forall i\in\Omega_{\text{bus}},\forall t\in\Omega_{\text{t}},\forall d\in\Theta \tag{30}$$

$$\begin{cases} P_{i,d,t}^{\text{in}} = P_{i,d,t}^{\text{sub}} + P_{i,d,t}^{\text{EVCS}} + P_{m,i,d,t}^{\text{MESS}} + P_{i,d,t}^{\text{DG}} - \sigma_{i,d,t}(P_{i,d,t}^{\text{l1}} + \\ P_{i,d,t}^{\text{l2}} + P_{i,d,t}^{\text{l3}}) \\ Q_{i,d,t}^{\text{in}} = Q_{i,d,t}^{\text{sub}} + Q_{i,d,t}^{\text{EVCS}} + Q_{m,i,d,t}^{\text{MESS}} + Q_{i,d,t}^{\text{DG}} - \sigma_{i,d,t}(Q_{i,d,t}^{\text{l1}} + \\ Q_{i,d,t}^{\text{l2}} + Q_{i,d,t}^{\text{l3}}) \end{cases} \tag{31}$$
$$\forall i \in \Omega_{\text{bus}}, \forall t \in \Omega_{\text{t}}, \forall d \in \Theta$$

where, R_{ij} and X_{ij} represent the resistance and reactance of line ij respectively; $Q_{i,d,t}^{\text{l1}}$, $Q_{i,d,t}^{\text{l2}}$ and $Q_{i,d,t}^{\text{l3}}$ are respectively the reactive power of the primary load, secondary load and tertiary load of node i in the t period under the extreme scenario d; $P_{ij,d,t}$ and $Q_{ij,d,t}$ are respectively the active power and reactive power of the line ijin the t period under the extreme scenario d; $V_{i,d,t}$ is the voltage of the node i in the t period under the extreme scenario d; $P_{i,d,t}^{\text{in}}$ and $Q_{i,d,t}^{\text{in}}$, $P_{i,d,t}^{\text{sub}}$ and $Q_{i,d,t}^{\text{sub}}$,$P_{i,d,t}^{\text{DG}}$and $Q_{i,d,t}^{\text{DG}}$, $P_{i,d,t}^{\text{EVCS}}$ and $Q_{i,d,t}^{\text{EVCS}}$ are respectively the real and reactive power injected by the node i in the t period under the extreme scenario d, the real and reactive power emitted by the substation connected to the node, the real and reactive power at the node i, and the real and reactive power injected by the EVCS at node i during period t under extreme scenario d; $Q_{m,i,d,t}^{\text{MESS}}$ represents the reactive power of the MESS m at the node$i$ during the period under extreme scenario d; $\sigma_{i,d,t}$ is the state variable of node i under extreme scenario d.

(5) Node voltage and branch current upper and lower limit constraints

Secure island operation requires maintaining nodal voltage and branch current magnitudes within their designated safe intervals:

$$\begin{cases} \sigma_{i,d,t}\left(V_i^{\min}\right)^2 \le V_{i,d,t}^2 \le \sigma_{i,d,t}\left(V_i^{\max}\right)^2, \\ \forall i \in \Omega_{\text{bus}}, t \in \Omega_{\text{t}}, \forall d \in \Theta \\ I_{ij,d,t}^2 \le Z_{ij,d,t}\bar{I}_{ij}^2, \\ \forall ij \in \Omega_{\text{line}}, \forall t \in \Omega_{\text{t}}, \forall d \in \Theta \end{cases} \tag{32}$$

where, $V_i^{\max}$, $V_i^{\min}$ and $\bar{I}_{ij}^2$ represent the upper and lower bounds of the voltage magnitude of node i and the square of the maximum allowable current amplitude for branch ij respectively.

(6) Black start DG operating constraints

$$\begin{cases} 0 \le P_{i,d,t}^{\text{DG}} \le P_{i,t}^{\text{DG, max}} \\ Q_{i,t}^{\text{DG, min}} \le Q_{i,d,t}^{\text{DG}} \le Q_{i,t}^{\text{DG, max}} \end{cases} \tag{33}$$
$$\forall i \in \Omega_{\text{DG}}, \forall t \in \Omega_{\text{t}}, \forall d \in \Theta$$

$$V_{i,d,t} = V_0, \forall i \in \Omega_{\text{DG}}, \forall t \in \Omega_{\text{t}} \tag{34}$$

where, $P_{i,t}^{\text{DG, max}}$,$Q_{i,t}^{\text{DG, min}}$and $Q_{i,t}^{\text{DG, max}}$ are respectively the maximum tolerable of active power output, the maximum tolerable of reactive power output and the minimum tolerable of reactive power output of black start DG at node i in period t; V_0 represents the rated voltage of black start DG.

(7) Line switch status constraints

Switching operation variables $S_{ij,d,t}^{\text{open}}$ and $S_{ij,d,t}^{\text{close}}$, along with the state variable $S_{ij,d,t}$ are introduced to constrain the operations of tie switches and sectionalizing switches during network reconfiguration and island merging.

a) Switch initial state constraints

All sectionalizing switches are assumed to be initially closed, and all tie switches are assumed to be initially open in period 1.

$$\begin{cases} S_{ij,d,1} = 1 ij \in \Omega_{\text{sec}} \\ S_{ij,d,1} = 0 ij \in \Omega_{\text{tie}} \end{cases}, \forall d \in \Theta \tag{35}$$

where, $S_{ij,d,1}$ is the switch status variable of line ij in period 1 under extreme scenario d.

b) Switch operation continuity constraints

$$S_{ij,d,t}^{\text{open}} - S_{ij,d,t}^{\text{close}} = S_{ij,d,t} - S_{ij,d,t-1}, \forall i \in \Omega_{\text{bus}}, \\ \forall t \in \Omega_{\text{t}}, \forall d \in \Theta \tag{36}$$

$$S_{ij,d,t}^{\text{open}} + S_{ij,d,t}^{\text{close}} \le 1, \forall ij \in \Omega_{\text{line}}, \forall t \in \Omega_{\text{t}}, \forall d \in \Theta \tag{37}$$

(8) Total switching operation constraints

To consider both switch lifespan and cost control, it is necessary to constrain the total number of switching operations.

$$\sum_{t\in\Omega_{\text{t}}}\sum_{ij\in\Omega_{\text{line}}}(S_{ij,d,t}^{\text{open}} + S_{ij,d,t}^{\text{close}}) \le N_{\max}, \forall d \in \Theta \tag{38}$$

where, $N_{\max}$ is the maximum allowable total number of switching operations.

(9) Tie line and line connection status constraints

An intermediate variable $A_{ij,d,t}$ is defined to indicate whether the line is affected by extreme disasters and whether it has been reinforced.

$$A_{ij,d,t} = u_{ij,d,t} + y_{ij}, \forall ij \in \Omega_{\text{line}}, \forall t \in \Omega_{\text{t}}, \forall d \in \Theta \tag{39}$$

where, $A_{ij,d,t}$ equals 1 if the line is unaffected by extreme disasters, or if it is affected but has been reinforced; otherwise, it equals 0.

The line connectivity constraints are：

$$Z_{ij,d,t} = A_{ij,d,t}S_{ij,d,t}, \forall ij \in \Omega_{\text{line}}, \forall t \in \Omega_{\text{t}}, \forall d \in \Theta \tag{40}$$

The line connectivity status depends on both the switch status and the intermediate variable. The line is connected if its switch is closed and the intermediate variable equals 1; otherwise, the line remains disconnected.

(10) MESS dynamic dispatch constraints

a) Connection status constraints

Only MESS units participating in pre-disaster pre-deployment can engage in dynamic dispatch during disasters, ensuring that each MESS connects to at most one node throughout the dispatch process.

$$\sum_{i\in\Omega_{\text{bus}}} x_{m,i,d,t} \le \sum_{i\in\Omega_{\text{bus}}} x_{m,i,0}, \forall m \in \Omega_{\text{MESS}}, \\ \forall t \in \Omega_{\text{t}}, \forall d \in \Theta \tag{41}$$

b) Movement time constraints

When relocating a MESS, the movement from node i to node j must satisfy the minimum movement time requirement. If the movement is incomplete within a given period, its connection status with any node remains 0.

$$x_{m,i,d,t} + x_{m,j,d,t+\tau} \le 1, \ \forall m \in \Omega_{\text{MESS}}, \forall d \in \Theta, \\ \forall i,j \in \Omega_{\text{bus}}, i \ne j, \\ \forall 1 \le t \le T - \Delta t_{m,i,j}, \forall 0 \le \tau \le \Delta t_{m,i,j} \tag{42}$$

c) Initial period dispatch location constraints

The location of each MESS at the initial dispatch period corresponds to its pre-deployed location.

$$x_{m,i,d,1} = x_{m,i,0}, \forall m \in \Omega_{\text{MESS}}, \forall i \in \Omega_{\text{bus}}, \forall d \in \Theta \tag{43}$$

d) MESS discharging constraints

Each MESS is fully charged during the pre-disaster pre-deployment stage and operates in unidirectional discharging mode during the in-disaster restoration phase.

$$0 \le P^{\mathrm{MESS}}_{m,i,d,t} \le x_{m,i,d,t} P^{\mathrm{MESS}}_{\max}, \forall m \in \Omega_{\mathrm{MESS}}, \forall i \in \Omega_{\mathrm{bus}}, \forall t \in \Omega_{\mathrm{t}}, \forall d \in \Theta \tag{44}$$

$$E^{\mathrm{MESS}}_{m,d,t} = E^{\mathrm{MESS}}_{m,d,t-1} - \sum_{i \in \Omega_{\mathrm{bus}}} P^{\mathrm{MESS}}_{m,i,d,t} \Big/ \eta^{\mathrm{dis}}_{m}, \forall d \in \Theta, \forall m \in \Omega_{\mathrm{MESS}}, \forall t \in \Omega_{\mathrm{t}}, t \ne 1, \tag{45}$$

$$E^{\mathrm{MESS}}_{m,d,0} = E^{\mathrm{MESS,\ max}}_{m}, \forall m \in \Omega_{\mathrm{MESS}}, \forall d \in \Theta \tag{46}$$

$$E^{\mathrm{MESS}}_{m,d,t} \ge E^{\mathrm{MESS,\ min}}_{m}, \forall m \in \Omega_{\mathrm{MESS}}, \forall t \in \Omega_{\mathrm{t}}, \forall d \in \Theta \tag{47}$$

where, $P^{\mathrm{MESS}}_{\max}$ is the maximum power of mobile storage unit m; η^{dis}_{m} is the discharge efficiency of mobile storage unit m; $E^{\mathrm{MESS}}_{m,d,t}$ is the power of mobile storage unit m in period t under extreme scenarios d; $E^{\mathrm{MESS,\ max}}_{m,d}$ is the maximum energy capacity of mobile storage unit m; $E^{\mathrm{MESS,\ min}}_{m}$ is the minimum allowable energy level of mobile storage unit m; $E^{\mathrm{MESS}}_{m,d,0}$ is the initial energy level of mobile storage unit m under extreme scenario d.

5. Case study

For performance evaluation of the proposed model, case studies are performed on a modified IEEE 33-bus distribution network, whose topology is shown in Fig. A1 of Appendix A. Relevant nodal load levels are provided in Table A1 of Appendix A, respectively. and the cost coefficients for shedding primary, secondary, and tertiary loads follow a ratio of 4:2:1, respectively. The locations and capacities of black-start DG are specified in Table A2 of Appendix A. MESS parameters are provided in Table A3 of Appendix A. Considering the short duration of the disaster restoration period, the lifetime degradation of the mobile energy storage system is not considered in this study. Other electrical parameters are consistent with Reference (Baran and Wu, 2002). Computational solutions for the mixed-integer linear programming (MILP) model were obtained via the GUROBI solver within the MATLAB 2022a platform. Based on the distribution of critical loads and considering synergistic complementarity with the MESS, EVCS are pre-deployed at nodes 3 and 11. Both nodes are primary load nodes without DG, allowing them to serve as fixed support points in space and form a coordinated "fixed-mobile" power supply network with the MESS pre-deployed at nodes 6 and 10.

To investigate the effectiveness within the proposed model in enhancing distribution network resilience, the following four cases are designed:

Case1: Pre-disaster line reinforcement is not considered; fault restoration during disasters relies solely on island partitioning and merging.

Case2: Pre-disaster line reinforcement is considered; fault restoration during disasters relies solely on network reconfiguration.

Case3: Pre-disaster line reinforcement is considered; fault restoration during disasters relies solely on island partitioning and merging.

Case4: The proposed model considers pre-disaster line reinforcement and MESS deployment, and performs fault restoration during disasters through coordinated strategies including power discharge from pre-deployed EVCS, dynamic MESS dispatch, island partitioning and merging, and network reconfiguration.

5.1. Strong wind path and distribution line failure rate analysis

To validate the effectiveness of the proposed model, an extreme wind disaster scenario with spatiotemporal evolution characteristics needs to be constructed. This study analyzes a hypothetical strong wind process with typical movement and evolution features, which can simulate a wide-area wind disaster triggered by events such as intense extratropical cyclones, characterized by a clear predominant direction and a high-intensity core region.

A spatial coordinate system with Node 1 as the origin is established within the distribution network topology, defining due east as the positive x-axis direction. The predominant direction of the strong wind field is set at a 150° angle to the positive x-axis. Its high-intensity wind zone is initially located southeast of the distribution network at coordinates (75 km, −75 km) and moves along the predominant direction at a speed of 7.5 km/h. Based on the strong wind field model established in Section 3.1, the calculated spatiotemporal failure rate distribution of the distribution lines is shown in Fig. 1.

As observed in Fig. 1, the spatiotemporal evolution of this strong wind process imposes two main impacts on the distribution network. The first impact arises from the initial passage of the high-intensity wind zone over the line corridors, where the rapid increase in wind speed causes the failure rate of some lines to reach its first peak. The second impact is induced by the renewed coverage of the line corridors by the high-intensity wind zone as the wind field moves, inflicting cumulative damage and a repeated shock on the distribution facilities, leading to a second, and typically higher, peak in the failure rate.

5.2. Reinforcement results and cost analysis

To compare the economics of different disaster prevention resource allocation strategies, the line reinforcement results for the four cases are shown in Table 2, and the cost comparisons are presented in Table 3.

As observed from Tables 2 and 3, in the pre-disaster prevention stage, Case 3 incorporates pre-disaster line reinforcement on the basis of Case 1. Although this increases the line reinforcement cost, it effectively restores load, thereby reducing the load shedding cost. This results in a total cost reduction of 50.70% compared to Case 1, demonstrating that pre-disaster line reinforcement can effectively ensure line connectivity and enhance system resilience while significantly lowering the total cost.

During the in-disaster response stage, Case 2 adopts a network reconfiguration strategy but still experiences significant load loss even with extensive line reinforcement. In contrast, Case 3 utilizes a DG island partitioning and merging strategy, forming new power supply areas to serve the shed loads. This approach saves 27.5% in line reinforcement costs compared to Case 2 while fully leveraging the power supply capability of black-start DG to effectively reduce load shedding costs. Consequently, the total cost of Case 3 decreases by 29.15% compared to Case 2, further validating that the DG island partitioning and merging restoration strategy during disasters can effectively reduce system load loss.

Building upon Case 3, Case 4 introduces the coordinated pre-disaster

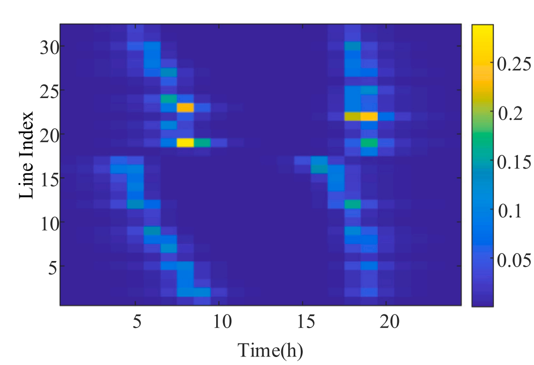

Fig. 1. Time-varying failure rate of distribution lines.

Table 2
Line reinforcement results under different cases.

Case	Reinforced Lines	MESS Pre-deployment Location
1	–	–
2	5,7,13,24	–
3	5,7,11,13	–
4	3,5,7,13	MESS1: Node 10 MESS2: Node 6

Table 3
Cost breakdown of the four cases.

Cost (yuan)	Case 1	Case 2	Case 3	Case 4
Reinforcement Cost	–	500000	362500	362500
Load Shedding Cost	7403940	4650960	3284340	190072
Switching Cost	9320	7360	7680	6480
MESS Fixed Cost	–	–	–	2000
MESS Mobility Cost	–	–	–	43508
MESS Operating Cost	–	–	–	4955
EVCS Discharge Cost				2160
Total Cost	7413260	5158320	3654520	611675

deployment of MESS and EVCS, along with precise dynamic dispatch during disasters. By directly supplying loads via MESS and EVCS, it maximizes the guarantee of system power supply. Although load restoration is not fully achieved in some scenarios, the total cost is ultimately reduced by 83.26% compared to Case 3. Furthermore, as shown in Table 3, the operational and mobilization costs of MESS account for a relatively small proportion of the total cost. Consequently, moderate fluctuations in unit costs do not significantly affect the robustness of the overall optimization results. Thereby validating that the proposed model, through the coordinated optimization of pre- and in-disaster resources, can significantly enhance system resilience while maintaining economic efficiency.

Based on the line failure rates, typical fault scenarios are generated via Monte Carlo simulation and subsequently reduced to three representative scenarios (Hajibandeh et al., 2018), with occurrence probabilities of 0.2160, 0.2316, and 0.5524, respectively. To analyze the results of the restoration models under the four cases, Fault Scenario 1, presented in Table 4, is taken as an example to examine the load loss, line connectivity, and island partitioning and merging outcomes.

5.3. Load shedding analysis

To validate the full-cycle load restoration capability of the proposed model under strong wind conditions, the load shedding amounts of the four cases under Fault Scenario 1 are listed in Table 5. The load shedding situations for the remaining two scenarios are provided in Appendix Table A5 and Table A6.

As illustrated in Table 5, compared to Case 1, Case 3 reduces the total load shedding by 94.94% through pre-disaster line reinforcement, demonstrating the effectiveness of pre-disaster preventive measures in restoring load supply. Compared to Case 2, Case 3 effectively restores all primary load using the DG island partitioning and merging strategy during disasters, achieving 100% restoration of primary load, although

Table 4
Fault scenario 1.

Period	Faulted Lines
3	5
5	5,13,16
7	5,13,16,7,19
18	5,13,16,7,19,12
19	5,13,16,7,19,12,18,29,25
20	5,13,16,7,19,12,18,29,25,11

Table 5
Comparison of load shedding among the four cases.

Load Shedding (kW)	Case 1	Case 2	Case 3	Case 4
Primary Load	504.90	2243.85	0	0
Secondary Load	3780.00	1238.4	504.6	0
Tertiary Load	6866.70	2425.2	59.4	0
Total Load Shedding	11151.6	5907.45	564	0

some secondary load remains unrestored. In contrast, the proposed Case 4 leverages the coordinated pre-disaster deployment of MESS and EVCS, combined with the synergistic effect of precise MESS dynamic dispatch and EVCS discharge support during disasters. This fully exploits the advantage of multi-source "mobile - fixed" power supply, enabling the restoration of all load in the area.

Furthermore, Tables A5 and A6 indicate that while Case 4 may not fully restore all tertiary load in a few extreme scenarios, it consistently achieves 100% reliable power supply for primary and secondary loads, performing significantly better than the other cases.

5.4. Analysis of line connectivity and DG island partitioning and merging results

For performance evaluation of the proposed framework in enhancing the system power supply capability through pre-disaster line reinforcement, EVCS pre-deployment, MESS pre-deployment, and in-disaster DG island partitioning and merging combined with real-time MESS dynamic dispatch, the line connectivity for Cases 1, 2, and 3 is presented in Table A4 of Appendix A, while the corresponding results for Case 4 are shown in Fig. 2.

As indicated in Table A4, Case 1 establishes new supply paths through DG island partitioning and merging. During periods 3–4, when few lines are faulted, the system meets the supply requirements without altering its topology. As the fault scale expands, supply is restored by closing tie switches to maintain connectivity in tie branches and performing DG island partitioning and merging. Case 2, with optimally reinforced lines L5, L7, L13, and L24, maximizes line connectivity and load restoration in Scenario 1. During periods 3 and 4, all system lines remain connected due to prior reinforcement; however, as the fault evolves, the supply paths formed by line reinforcement and network reconfiguration are limited, resulting in numerous line disconnections and significant load loss. Case 3 enhances Case 1 by adding pre-disaster reinforcement of lines L5, L7, L11, and L13 to ensure supply to critical loads. During periods 5–17, line connectivity is maintained through prior reinforcement, and the operation of tie switches enables DG1, DG2, DG3, and DG4 to form a large supply area, restoring all loads within it. Benefiting from the earlier island merging strategy, the system largely avoids an increase in load-shedding nodes when new line faults occur later. However, in period 19, the failure of line 18 disconnects both sides of node 19, causing load loss at this node.

As shown in Fig. 2, Case 4 builds upon Case 3 by incorporating pre-disaster MESS pre-deployment and in-disaster dynamic dispatch. When both sides of node 19 are faulted under strong wind conditions, the system successfully restores power to this node by dispatching MESS2 in real time. Furthermore, when the power transmitted by DG2 and tie line L35 is insufficient to supply the critical loads at nodes 10 and 11, MESS2 is dispatched to node 10 to provide support. This further verifies that the proposed model achieves system-wide power restoration at minimal economic cost. It is noteworthy that although the island merging status is identical in some periods across all four cases, the extent of the supply areas formed in coordination with the substation differs.

5.5. Analysis of MESS deployment, dispatch, and discharging

This paper assumes a travel speed of 30 km/h for the MESS. Calculations show that MESS units can be emergently dispatched between

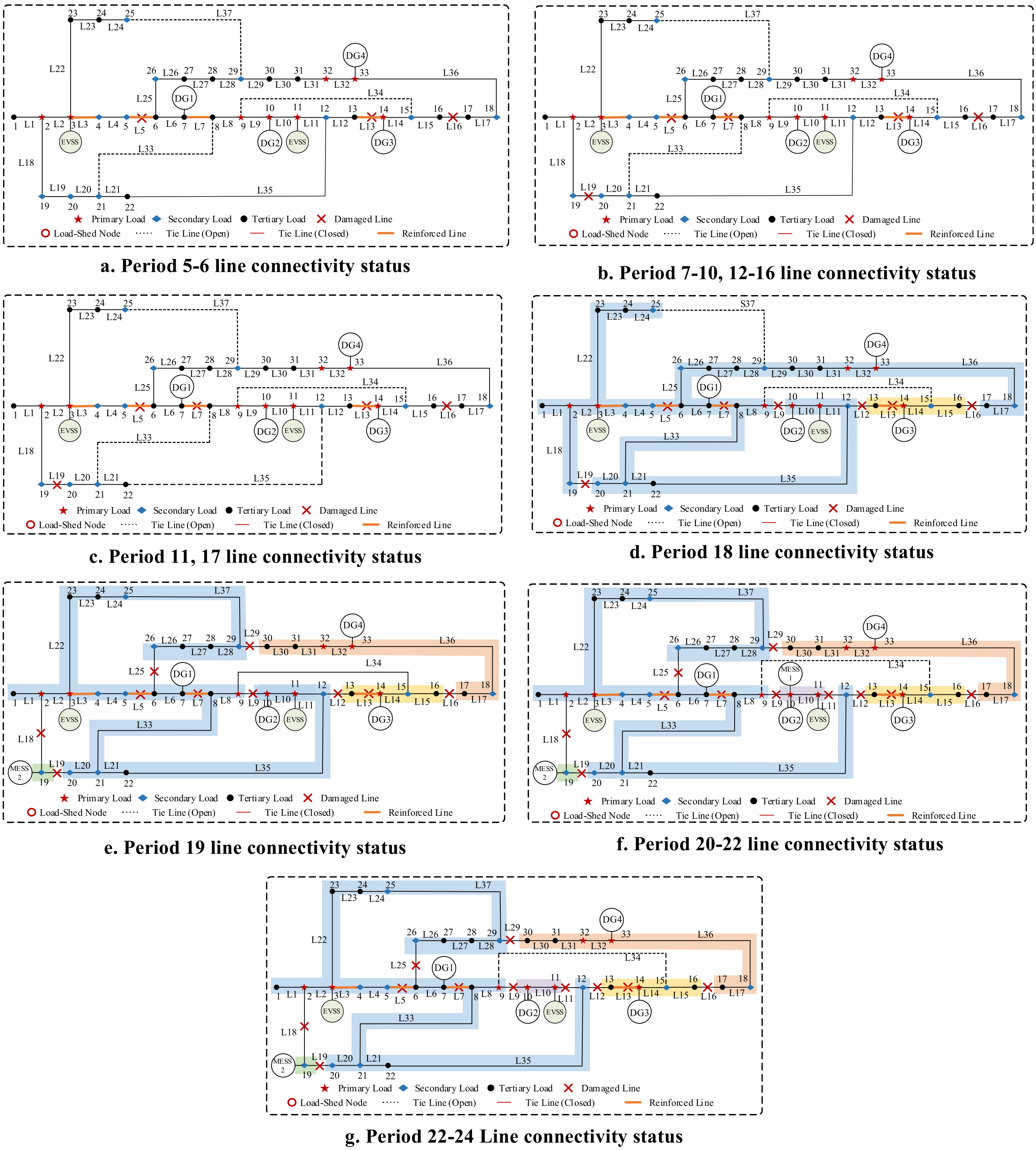

Fig. 2. Line connectivity status of case 4.

most nodes within a short time. In Case 4, the pre-deployment and dynamic dispatch locations of MESS1 and MESS2 are shown in Fig. 3, and their discharging behaviours are shown in Fig. 4.

As observed in Fig. 3, MESS1 is optimally pre-deployed at node 10 and remains there throughout periods 1–24 to balance cost and load restoration. MESS2 is optimally pre-deployed at node 6; it is dispatched to node 21 from period 2 to period 12, then to node 20 from period 13 to period 18, and finally to node 19 in period 19. Fig. 4 indicates that MESS1 and MESS2 adopt dynamic discharging strategies to maintain economic efficiency.

As shown in Fig. 4(a), after MESS1 is stationed at node 10, in period 20 when the primary load demand increases, it supplies power together with DG2 to the loads at nodes 10 and 11, following a power-balancing strategy where the sum of the discharge powers from DG2 and MESS1 plus the transmission power from the tie line equals the total load demand at nodes 10 and 11. In Fig. 4(b), MESS2 begins supplying the load at node 19 in period 19 after line L18 fails. It remains in a non-discharging state during dispatch prior to period 19 to reduce

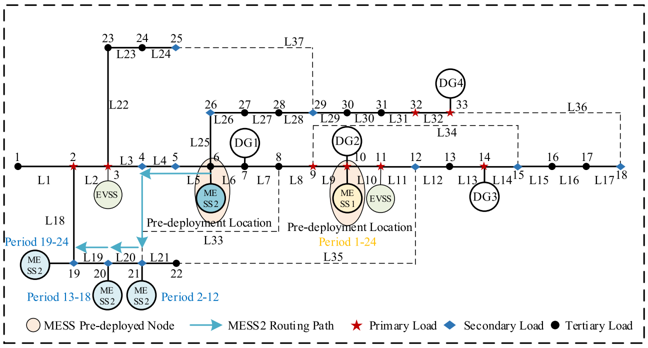

Fig. 3. MESS pre-deployment and dispatch locations.

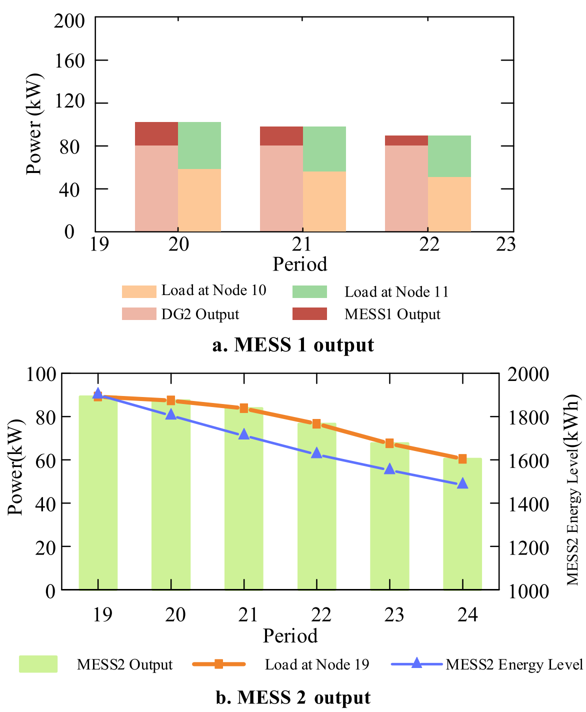

Fig. 4. MESS output status.

operating costs. In period 19, it implements a power-balancing strategy according to the load demand at node 19, with its discharge power profile synchronizing with the load power curve. This demonstrates that MESS dispatch can cooperate effectively with DG island partitioning and merging to restore system power supply and enhance resilience.

6. Conclusion

This paper proposes an optimization method for enhancing distribution network resilience, integrating pre-disaster line reinforcement, coordinated EVCS and MESS deployment, in-disaster DG island partitioning and merging, and MESS dynamic dispatch. A coordinated optimization framework spanning pre-disaster prevention and in-disaster response is established. Data from the simulations provide evidence that:

(1) The core capability of the coordinated optimization model lies in its capacity to identify system vulnerabilities under extreme strong wind disasters. By combining the flexibility of MESS with the fixed support capability of EVCS pre-deployed at critical nodes, a hybrid mobile-fixed multi-source coordinated power supply mode is formed. This mode significantly enhances the system's complementary capability and restoration robustness during fault evolution, achieving 100% restoration of both primary and secondary loads in typical fault scenarios.

(2) The coordinated operation of dynamic MESS dispatch and the DG island merging mechanism during disasters enables flexible expansion of the power supply range and precise load restoration under fault scenarios. This strategy delivers a resilient power supply while ensuring cost-effectiveness reducing the total cost of the proposed case by 83.3% compared to the case considering pre-disaster line hardening and restoration solely via in-disaster island partitioning and merging.

Future research will further incorporate transportation-power system coupling effects, introduce road network capacity constraints and disaster-induced path disruption risks, and deepen the robust optimization of coordinated MESS dispatch paths and EVCS operation strategies under extreme weather conditions. In addition, considering the potential computational burden of the MILP model in large-scale systems, future work will also investigate decomposition algorithms to further balance model complexity and solution efficiency.

CRediT authorship contribution statement

Jie Ma: Writing – review & editing, Validation, Methodology, Funding acquisition, Conceptualization. **Youwen Zhang:** Writing – review & editing, Methodology, Formal analysis, Data curation. **Changqing Xu:** Supervision, Methodology, Investigation, Conceptualization. **Yong Guo:** Validation, Supervision, Investigation. **Yihao Sun:** Writing – original draft, Validation, Conceptualization.

Declaration of Competing Interest

The authors declare that they have no known competing financial interests or personal relationships that could have appeared to influence the work reported in this paper.

Acknowledgments

This work is supported by the State Grid Henan Economic Research Institute Science and Technology Project "Calculation and Demonstration of Distributed Photovoltaic Open Capacity Based on Multi-Source Heterogeneous Data" (5217L0230013).

Appendix A

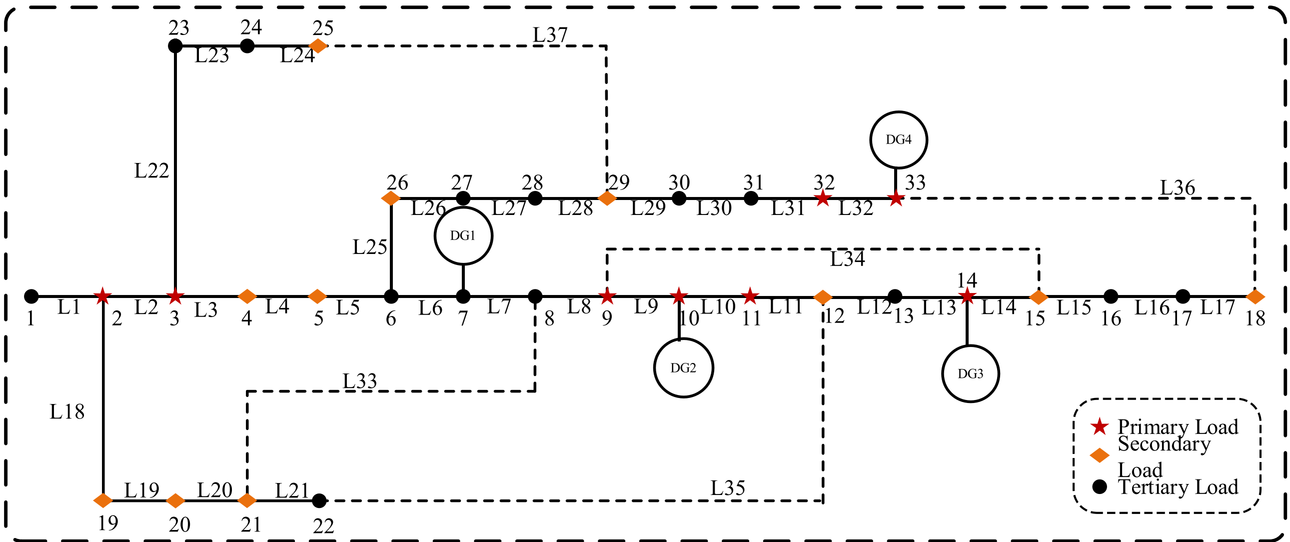

Fig. A1. Configuration diagram for the revised IEEE 33-node test feeder

Table A1
Load classification

Load Category	Node Numbers
Primary Load	2,3,9,10,11,14,32,33
Secondary Load	4,5,12,15,18,19,20,21,25,26,29
Tertiary Load	6,7,8,13,16,17,22,23,24,27,28,30,31

Table A2
Black-start DG parameters

DG Name	Connected Node	Rated Capacity (kW)
DG1	7	20
DG2	10	80
DG3	14	310
DG4	33	900

Table A3
MESS parameters

Parameter	Value
Fixed Cost	1000 Yuan
Mobility Cost	30 Yuan /km
Discharging Cost	0.6 Yuan /kWh
Moving Speed	30 km/h
Rated Power	400 kW
Rated Capacity	2000 kWh
Discharging Efficiency	0.9

Table A4
Line connectivity status for cases 1–3

Case	Period	Faulted Lines	Disconnected Branches
Case 1	3–4	5	33,34,35,36,37
	5–6	5,13,16	33,34,37
	7	5,13,16,7,19	33,37
	8	5,13,16,7,19	33
	9,11–17	5,13,16,7,19	33,35
	18	5,13,16,7,19,9,12	None
	19	5,13,16,7,19,9,12,18,25,29	None
	20–24	5,13,16,7,19,9,12,18,25,29,11	33,35
Case 2	5–6	16	33,34,35,37
	7,9–13,15–17	16,19	34,35,37
	8,14	16,19	33,34,37
	18	16,19,9,12	37
	19	16,19,9,12,18,25,29	36
	20–24	16,19,9,12,18,25,29,11	36
Case 3	5–6	16	33,34,35,37
	7	16,19	34,35,37
	8–17	16,19	33,34,37
	18	16,19,9,12	34,37
	19	16,19,9,12,18,25,29	34
	20	16,19,9,12,18,25,29	None
	21–23	16,19,9,12,18,25,29	34
	24	16,19,9,12,18,25,29	34,35

Note: "+ " represents island merging.

Table A5
Load shedding comparison of the four cases under scenario 2

Load Shedding (kW)	Case 1	Case 2	Case 3	Case 4
Primary Load	1224.4	1791.9	0	0
Secondary Load	2533.5	553.5	2631.9	0
Tertiary Load	4003.1	3129.3	2704.8	0
Total Load Shedding	7761.0	5474.7	5336.7	0

Table A6
Load shedding comparison of the four cases under scenario 3

Load Shedding (kW)	Case 1	Case 2	Case 3	Case 4
Primary Load	0	1521.5	0	0
Secondary Load	0	928.85	504.6	0
Tertiary Load	7634.7	2425.2	0	961.0
Total Load Shedding	7634.7	4875.55	504.6	961.0

Data availability

The authors do not have permission to share data.

References

Abbasi, A.R., Seifi, A.R., 2015. Considering cost and reliability in electrical and thermal distribution networks reinforcement planning[J]. Energy 84, 25–35.
Alizadeh, A., Kamwa, I., Cao, B., et al., 2024. A novel model for tight radiality constraints incorporating dynamic parent–child selection and single commodity flow: an application of microgrid formation[J]. Electr. Power Syst. Res. 231, 110332.
Baran, M.E., Wu, F.F., 2002. Network reconfiguration in distribution systems for loss reduction and load balancing[J]. IEEE Trans. Power Deliv. 4 (2), 1401–1407.
Chen, T., Xu, X., Wang, H., et al., 2022. Routing and scheduling of mobile energy storage system for electricity arbitrage based on two-layer deep reinforcement learning[J]. IEEE Trans. Transp. Electrification 9 (1), 1087–1102.
El-Sayed, W., Awad, A., Azzouz, M., et al., 2025. Mobile energy storage for inverter-dominated isolated microgrids resiliency enhancement through maximizing loadability and seamless reconfiguration[J]. Prot. Control Mod. Power Syst. 10 (4), 89–102.
Gupta, Y., Nellikkath, R., Chatterjee, K., et al., 2021. Volt–Var optimization and reconfiguration: Reducing power demand and losses in a droop-based microgrid[J]. IEEE Trans. Ind. Appl. 57 (3), 2769–2781.
Hajibandeh, N., Shafie-khah, M., Talari, S., et al., 2018. Demand response-based operation model in electricity markets with high wind power penetration[J]. IEEE Trans. Sustain. Energy 10 (2), 918–930.
Hao, G., Li, Y., Li, Y., et al., 2025. Safe reinforcement learning for active distribution networks reconfiguration considering uncertainty[J]. IEEE Trans. Ind. Appl. 61 (1), 1757–1769.
He, Y., Fu, H., Wu, A.Y., et al., 2025. Enhancing resilience of distribution system under extreme weather: two-stage energy storage system configuration strategy based on robust optimization[J]. Int. J. Electr. Power & Energy Syst. 167, 110624.
Huang, M., Shen, H., Peng, J., et al., 2022. Research on fault recovery method of AC/DC hybrid distribution network with electric vehicle charging station[J]. Energy Rep. 8, 273–279.
Lei, S., Chen, C., Song, Y., et al., 2020. Radiality constraints for resilient reconfiguration of distribution systems: Formulation and application to microgrid formation[J]. IEEE Trans. Smart Grid 11 (5), 3944–3956.
Li, X., Shi, Y., Zhang, R., et al., 2025. Research on the integration of mobile energy storage system for enhancing black start capability and resilience in distribution networks under extreme events[J]. Sustain. Energy Grids Netw., 101724
Li, Y., Feng, B., Li, G., et al., 2018a. Optimal distributed generation planning in active distribution networks considering integration of energy storage[J]. Appl. Energy 210, 1073–1081.
Li, Y., Yang, Z., Li, G., et al., 2018b. Optimal scheduling of isolated microgrid with an electric vehicle battery swapping station in multi-stakeholder scenarios: a bi-level programming approach via real-time pricing[J]. Appl. Energy 232, 54–68.

Li, Y., Han, M., Yang, Z., et al., 2021. Coordinating flexible demand response and renewable uncertainties for scheduling of community integrated energy systems with an electric vehicle charging station: A bi-level approach[J]. IEEE Trans. Sustain. Energy 12 (4), 2321–2331.

Li, Y., Feng, B., Wang, B., et al., 2022. Joint planning of distributed generations and energy storage in active distribution networks: a bi-level programming approach[J]. Energy 245, 123226.

Li, Y., Lei, S., Sun, W., et al., 2023. A distributionally robust resilience enhancement strategy for distribution networks considering decision-dependent contingencies[J]. IEEE Trans. Smart Grid 15 (2), 1450–1465.

Liu, X., Wang, H., Sun, Q., et al., 2022. Research on fault scenario prediction and resilience enhancement strategy of active distribution network under ice disaster[J]. Int. J. Electr. Power & Energy Syst. 135, 107478.

Meng, Q., Tong, X., Hussain, S., et al., 2024. Revolutionizing photovoltaic consumption and electric vehicle charging: a novel approach for residential distribution systems [J]. IET Gener. Transm. & Distrib. 18 (17), 2822–2833.

Meng, Q., He, Y., Hussain, S., et al., 2025. Day-ahead economic dispatch of wind-integrated microgrids using coordinated energy storage and hybrid demand response strategies[J]. Sci. Rep. 15 (1), 26579.

Najafi, J., Anvari-Moghaddam, A., Mehrzadi, M., et al., 2021. An efficient framework for improving microgrid resilience against islanding with battery swapping stations[J]. IEEE Access 9, 40008–40018.

Peng, Z., Zhang, W., Xu, W., et al., 2024. Conditional value at risk-based island partitioning and fault restoration reconfiguration of active distribution networks[J]. Front. Energy Res. 12, 1460894.

Qian, T., Fang, M., Hu, Q., et al., 2025. V2Sim: an open-source microscopic V2G simulation platform in urban power and transportation network[J]. IEEE Trans. Smart Grid.

Qin, C., Lu, J., Zeng, Y., et al., 2024. Optimal two-stage dispatch method of distribution network emergency resources under extreme weather disasters[J]. Sustain. Energy Grids Netw. 38, 101321.

Qiu, D., Wang, Y., Wang, J., et al., 2023. Resilience-oriented coordination of networked microgrids: a shapley Q-value learning approach[J]. IEEE Trans. Power Syst. 39 (2), 3401–3416.

Sabouhi, H., Doroudi, A., Fotuhi-Firuzabad, M., et al., 2021. Electricity distribution grids resilience enhancement by network reconfiguration[J]. Int. Trans. Electr. Energy Syst. 31 (11), e13047.

Saif, A., Dimyati, K., Noordin, K.A., et al., 2023. Skyward bound: empowering disaster resilience with multi-UAV-assisted B5G networks for enhanced connectivity and energy efficiency[J]. Internet Things 23, 100885.

Shabani, A., Nafar, M., Niknam, T., 2025. Four-level framework for enhancing active distribution network resilience to wind storms[J]. Electr. Power Syst. Res. 249, 112027.

Shi, Q., Li, F., Dong, J., et al., 2022. Co-optimization of repairs and dynamic network reconfiguration for improved distribution system resilience[J]. Appl. Energy 318, 119245.

Shi, W., Liang, H., Bittner, M., 2023. Stochastic planning for power distribution system resilience enhancement against earthquakes considering mobile energy resources[J]. IEEE Trans. Sustain. Energy 15 (1), 414–428.

Wang, Z., Ding, T., Mu, C., et al., 2023. A distributionally robust resilience enhancement model for transmission and distribution coordinated system using mobile energy storage and unmanned aerial vehicle[J]. Int. J. Electr. Power & Energy Syst. 152, 109256.

Wu, C., Zhou, D., Lin, X., et al., 2022. A novel energy cooperation framework for multi-island microgrids based on marine mobile energy storage systems[J]. Energy 252, 124060.

Xu, G., Guo, Z., 2024. Resilience enhancement of distribution networks based on demand response under extreme scenarios[J]. IET Renew. Power Gener. 18 (1), 48–59.

Xu, Y., Wu, T., Hu, P., et al., 2025. Fault recovery method for distributed distribution network based on Island partition[J]. J. Electr. Eng. & Technol. 20 (1), 23–35.

Zhao, S., Li, K., Yin, M., et al., 2024. Transportable energy storage assisted post-disaster restoration of distribution networks with renewable generations[J]. Energy 295, 131105.

Zhou, J., Zhang, H., Cheng, H., et al., 2025a. Resilience-oriented transmission expansion planning under hurricane impact considering vulnerable line identification and hardening[J]. Prot. Control Mod. Power Syst. 10 (3), 98–113.

Zhou, J., Wu, X., Zhang, X., et al., 2025b. Resilience-oriented distributed generation planning of distribution network under multiple extreme weather conditions[J]. Sustain. Energy Grids Netw. 42, 101675.

Zhou, W., Zhao, P., Lu, Y., 2023. Collaborative optimal configuration of a mobile energy storage system and a stationary energy storage system to cope with regional grid blackouts in extreme scenarios[J]. Energies 16 (23), 7903.

Zhu, N., Wu, G., Chen, H., et al., 2025. Resilience enhancement for distribution networks under typhoon-induced multi-source uncertainties[J]. Energies 18 (13), 3394.

Ziari, I., Ledwich, G., Ghosh, A., et al., 2012. Optimal distribution network reinforcement considering load growth, line loss, and reliability[J]. IEEE Trans. Power Syst. 28 (2), 587–597.